Pre and Post-fault Current Control of Dual Three-Phase Reluctance Synchronous Drives

Hisham M. Eldeeb, Ayman S. Abdel-Khalik, *Senior Member, IEEE*, J. Kullick, Christoph M. Hackl, *Senior Member, IEEE*

***Abstract*—This paper presents the pre- and post-fault stator current control structures for symmetrical dual three-phase reluctance synchronous machines (SDT-RSMs) with different neutral-point configurations. The effect of winding chording and rotor saliency on the space harmonic mapping among different subspaces is investigated. This proves on one hand that the control structure in the pre-fault case can be simplified, while on the other hand shows that the derived harmonic mapping in literature is insufficient to ensure high performance operation in the post-fault operation. Moreover, the machine non-linearities are identified, through which the maximum-torque-per-ampere (MTPA) loci are obtained and employed in the pre- and post-fault cases. The theoretical findings are corroborated with finite element simulations and experimental validations on a 3 kW SDT-RSM prototype.**

***Index Terms*—Dual three phase, current control, fault tolerant, reluctance synchronous machine, space harmonics.**

NOMENCLATURE

Notation

$\mathbb{R}, \mathbb{N}$	Set of real, natural numbers
$n, m \in \mathbb{N}$	Number of rows, columns
$v \in \mathbb{R}$	Real scalar
$\boldsymbol{v} \in \mathbb{R}^n$	Real vector (bold), i.e. $\boldsymbol{v} = (v_1, v_2, ..., v_n)^\top$
$\|\boldsymbol{v}\|$	Euclidean norm of $\boldsymbol{v}$
$\|\boldsymbol{v}\|_\infty$	Supreme norm of $\boldsymbol{v}$, i.e. $\|\boldsymbol{v}\|_\infty = \max\{|v_1|, |v_2|, ..., |v_n|\}$
$\boldsymbol{V} \in \mathbb{R}^{n \times m}$	Real matrix (capital bold)

Subscripts and superscripts

$\square^\top$	Transpose operator for vectors or matrices
$\square_\mathrm{s}$	's' denotes referencing to the stator
$\square_\mathrm{s}^{\Lambda\lambda}$	'Λ' and 'λ' are arbitrary variables representing the coordinates of a subspace (i.e. $\Lambda\lambda \in \{\alpha\beta, dq, XY, xy, 0^+0^-\}$)

General

$\boldsymbol{T}_\mathrm{VSD} \in \mathbb{R}^{6 \times 6}$	Vector space decomposition matrix
$\boldsymbol{T}_\mathrm{p}(\phi) \in \mathbb{R}^{2 \times 2}$	Park's transformation with angle $\phi \in \mathbb{R}$
$\boldsymbol{T}_k \in \mathbb{R}^{6 \times 2}$	Optimization matrix
$k_\delta^\alpha, k_\delta^\beta$	Scalar optimization parameters in $\boldsymbol{T}_k$ of the $\delta \in \{X, Y\}$ coordinate
$\boldsymbol{J} \in \mathbb{R}^{2 \times 2}$	Rotation matrix, where $J := \boldsymbol{T}_\mathrm{p}(\frac{\pi}{2})^{-1}$

u	Electrical voltage (V)
i	Electrical current (A)
$\hat{i}$	Electrical current amplitude at steady-state (A)
ψ	Flux linkage (Wb)
$\boldsymbol{v}_\mathrm{s}^{a_1 \to c_2} \in \mathbb{R}^6$	Stator space vector in the $(\mathrm{a_1 b_1 c_1}\text{-}\mathrm{a_2 b_2 c_2})$ frame, where $\boldsymbol{v} \in \{\boldsymbol{u}, \boldsymbol{\psi}, \boldsymbol{i}\}$
m_e	Electromechanical torque (N·m)
m_load	Load torque (N·m)
n_p	Pole-pair number
ω_e	Electrical angular speed (rad/s)
ϕ_e	Electrical angular position (rad)
Θ	Mechanical inertia (kg·m^2)
σ	Phase shift between the windings $\mathrm{a_1 b_1 c_1}$ and $\mathrm{a_2 b_2 c_2}$ (rad)
R_s	Stator electrical resistance (Ω)
$\boldsymbol{L}_\mathrm{s}^{\Lambda\lambda} \in \mathbb{R}^{2 \times 2}$	Inductance matrix of the $\Lambda\lambda$ subspace (H)
$L_\mathrm{s}^\Lambda, L_\mathrm{s}^\lambda$	Inductance of the Λ- and λ-axis (H)
$L_\mathrm{m}^{\Lambda\lambda}$	$\Lambda\lambda$ cross-coupling inductance (H)

I. INTRODUCTION

THE rapid development in power electronic components and embedded systems over the last decade expedited the adoption of multi-phase drives, especially with their power-segmentation capability and the emergence of critical applications, requiring high levels of fault tolerance [1]. In particular, dual three-phase (DT) drives received significant attention, due to their relatively simple realization through rewinding of standard three-phase machines and adopting two off-the-shelf three phase inverters [2]–[8]. In literature, the DT windings are embedded in the stator slots, while attaining a specific spatial phase shift σ between the windings: 0 (rad) [8], $\pi/6$ (rad) asymmetrical [5], [6], [8], or $\pi/3$ (rad) symmetrical arrangements [7]. Although the asymmetrical configuration is the common type in literature, owing to its high quality flux linkage, it is not guaranteed that such winding configuration is feasible for all machines; since it depends on the number of stator slots per pole. On the other hand, the symmetrical configuration is not only realizable from any three-phase machine, but can also generate in some cases higher levels of electromechanical torque in post-fault operation [8]. Therefore, the symmetrical DT (SDT) case is considered in this paper.

The most common types of DT machines are induction and permanent magnet synchronous machines (PMSMs). Irrespective from the rotor type, a distinct feature of DT drives is the necessity of employing harmonic regulators; to ensure the flow of harmonic-free stator currents and, thus, minimize the torque ripples [4], [6]. With the available body of literature, it is clear that the current control structure is identical for

machines with similar σ, where the rotor type contributes only to the magnitude of harmonic currents [7], [9].

With the present thrive of efficiency enhancements and curtailing the dependance on rare earth elements, a proliferation of adopting reluctance synchronous machines (RSMs) in several applications has been reported [10], [11]. To the best of the authors' knowledge, the adoption of RSMs in multiphase applications, in particular SDT-RSMs, is seldomly studied for either the healthy or post-fault (i.e. post open-phase faults) cases. Attaining a high performance current regulator is essential not only for the healthy operation, but also in post-fault case, where the current regulator is the underlying controller to post-fault optimization strategies [8], [12]. Thus, it is of interest to investigate if the presented generalized current controller structure for SDT drives in [7] would be applicable to SDT-RSMs. Upon implementing the controller in [7] and the post-fault strategy for SDT drives in [8], the post-fault results indicated the presence of *unexpected* low-order harmonic currents in the non-torque producing subspaces, which is translated to high torque ripples accompanied with significant acoustic noise. Additionally, it is worth to mention that the known highly non-linear properties of RSMs, as in [11], could give rise to further complications from a current controller design perspective; impacting the effectiveness of the post-fault operation. Furthermore, such generalized approach in [7] did not consider the impact of rotor saliency and the winding layout, in particular full-pitched and chorded windings, when studying the harmonic mapping to the different subspaces. In other words, the study of harmonic mapping was limited to compensating the harmonics present in the stator currents without either scrutinizing the impact of the winding layout or even elucidating the possibility of inhibiting the air-gap flux harmonics during the rewinding process.

As an attempt to fill this literature gap, this paper proposes the adoption of SDT-RSMs coupled with the following contributions:

- In-depth study concerning the impact of the windings configuration (chorded and full-pitched) and rotor saliency on the harmonic mapping to the different control subspaces. It is also pointed out that the rewinding process can be carried-out in a manner that simplifies the controller structure in the healthy case. Thus, reducing the complexity and correspondingly the computation burden;
- Computing the non-linear flux linkages. Such identification would not only contribute in enhancing the current controller dynamics, but also ensures minimum stator copper losses through the identification of the maximum-torque-per-ampere (MTPA) loci. Such loci account for the machine non-linearities without the need of conducting finite element (FE) simulations; and
- The state of the art post-fault optimization strategy, also known as the minimum-loss full range (MLFR), is applied to the SDT-RSM. Such strategy is available in literature only for asymmetrical DT drives. Moreover, only through the identified MTPA loci one can ensure maximum efficiency operation in the post-fault case.

This paper is organized as follows: Section II studies the
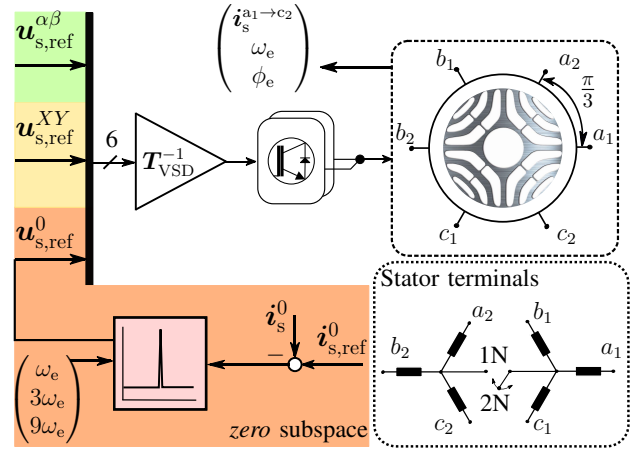
Fig. 1. SDT-RSM current control structure, where the $\alpha\beta$ and XY controllers are shown in Fig. 4 based on the discussions in Section II-B and Section III.

harmonic mapping to the different subspaces. Section III identifies the non-linear flux linkages and computes the MTPA loci. Section IV is the proposed current controller and its comparison with the generalized controller in [7]. Section V discusses the post-fault optimization and finally Section VI depicts the experimental results on a 3kW SDT-RSM prototype.

II. HARMONIC MAPPING IN SDT-RSM DRIVES

For SDT drives, the vector space decomposition (VSD) transformation [7],

$$\boldsymbol{T}_{\text{VSD}} = \frac{1}{3}\begin{bmatrix} 1 & -\frac{1}{2} & -\frac{1}{2} & \frac{1}{2} & -1 & \frac{1}{2} \\ 0 & \frac{\sqrt{3}}{2} & -\frac{\sqrt{3}}{2} & \frac{\sqrt{3}}{2} & 0 & -\frac{\sqrt{3}}{2} \\ 1 & -\frac{1}{2} & -\frac{1}{2} & -\frac{1}{2} & 1 & -\frac{1}{2} \\ 0 & -\frac{\sqrt{3}}{2} & \frac{\sqrt{3}}{2} & \frac{\sqrt{3}}{2} & 0 & -\frac{\sqrt{3}}{2} \\ 1 & 1 & 1 & 0 & 0 & 0 \\ 0 & 0 & 0 & 1 & 1 & 1 \end{bmatrix}, \quad (1)$$

decomposes the symmetrical six-phases quantities $\boldsymbol{v}_{\text{s}}^{a_1 \to c_2}$ to three orthogonal planes $(\boldsymbol{v}_{\text{s}}^{\alpha\beta}, \boldsymbol{v}_{\text{s}}^{XY}, \boldsymbol{v}_{\text{s}}^{0})^\top = \boldsymbol{T}_{\text{VSD}}\boldsymbol{v}_{\text{s}}^{a_1 \to c_2} = \boldsymbol{v}_{\text{s,VSD}}$, namely the equivalent $\alpha\beta$ subspace governing the electromechanical energy conversion, the XY subspace, which has a direct influence in ensuring optimum post-fault operation, and 0^+0^- in the "0" subspace representing the *zero* sequence components from both three-phase sets [8], [13]–[15]. It is essential to identify and compensate for the dominant harmonics per subspace; to ensure high performance with minimum torque ripples. The general structure of a SDT drive current controller is depicted in Fig. 1. Based on the developed harmonic mapping for the $\alpha\beta$ and XY subspaces in Section II-B, their corresponding harmonic regulators are identified and augmented to their fundamental controllers shown later in Section IV. The laid out controller for the *zero* subspace in Fig. 1 is explained next.

A. Triplet harmonics

The current $\boldsymbol{i}_{\text{s}}^{0}$ would only flow if the neutral point connector in Fig. 1 switches from the double neutral (2N) to the single neutral point (1N) configuration, which is only of interest in
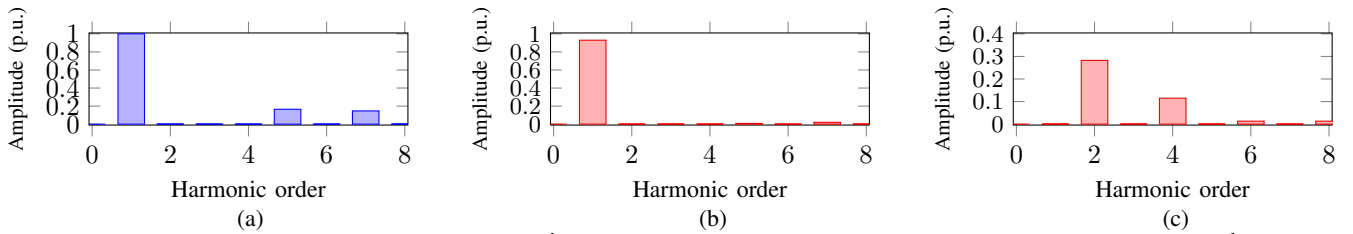
Fig. 2. MMF spectrum of (a) full pitched windings under $\|i_\mathrm{s}^{dq}\| = 1$ p.u. excitation and 7/9 chorded windings configuration at (b) $\|i_\mathrm{s}^{dq}\| = 1$ p.u., $i_\mathrm{s}^{xy} = \mathbf{0}_2$ and (c) $i_\mathrm{s}^{dq} = \mathbf{0}_2$, $\|i_\mathrm{s}^{xy}\| = 1$ p.u. excitations.
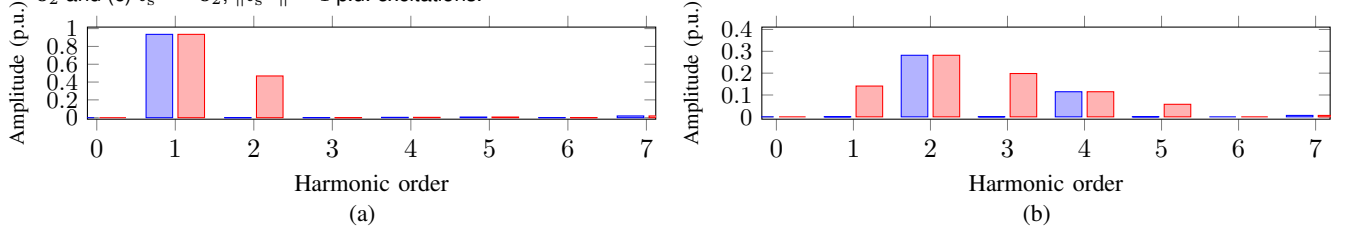
Fig. 3. Air-gap flux density spectrum of 7/9 chorded windings with **uniform** (in ▢) and **salient** (in ▢) air-gaps at (a) $\|i_\mathrm{s}^{dq}\| = 1$ p.u., $i_\mathrm{s}^{xy} = \mathbf{0}_2$ and (b) $i_\mathrm{s}^{dq} = \mathbf{0}_2$, $\|i_\mathrm{s}^{xy}\| = 1$ p.u. excitations.

the post-fault operation [8], [15]. In the post-fault case, the 1N configuration increases the torque per ampere capability (i.e. higher torque production) of the drive in comparison with the 2N case [8]. As discussed later in Section V, the reference current $i_\mathrm{s,ref}^0$ represents forced fundamental currents that would ultimately lead to optimal post-fault operation [15]. With respect to the harmonics present in the *zero* subspace, it can be concluded from [4], [7], [9] that the *zero* subspace is identical to asymmetrical drives in terms of the mapped triplets harmonics to such subspace. Such triplets harmonics are given by $3h$, such that $h \in \{1, 3, 5, ...\}$, where the 3rd and 9th harmonics are the dominant components. Based on the previous discussion, the *zero* subspace controller in Fig. 1, highlighted in ▢ , is enabled only in the post-fault case and composed of harmonic regulators tuned at the fundamental frequency, 3rd and 9th harmonics (i.e. ω_e, $3\omega_\mathrm{e}$, $9\omega_\mathrm{e}$). In the healthy case with 2N connection, the *zero* sequence controller is disabled.

B. Non-triplet harmonics

As far as six-phase machines are considered in this work, it is well-known that SDT windings have a $\pi/3$ phase belt similar to conventional three-phase windings [16]. Therefore, the SDT characteristics are essentially the same as a standard three-phase machine [17]. For the asymmetrical six-phase case, the phase belt is however reduced to $\pi/6$ by splitting the phase belt of a three-phase winding into two halves. This is why it is commonly called in literature as a split-phase dual three-phase winding [16]. It is a matter of fact that the air-gap distribution contains numerous harmonic components, among them are the phase belt harmonics of order [17]

$$k = \frac{2\pi\, l}{\sigma} \pm 1, \tag{2}$$

where σ is the phase belt angle and $l \in \mathbb{N}$ is a factor that depends on σ. Hence, in an asymmetrical DT winding with $\sigma = \pi/6$, the lowest order harmonics will be the 11th and 13th. While for a SDT with $\sigma = \pi/3$, the lowest order harmonics will be the 5th and 7th similar to a standard three-phase machine [7], [17]. Hence, the asymmetrical six-phase

winding corresponds to a much better flux distribution at a relatively high synchronous winding factor. On the other hand, a suitable coil chording for six phase drives should be considered to not only improve the flux distribution, suppress low order harmonics (LOHs) and reduce the leakage inductances [16], but also to improve especially the RSM performance under field weakening operation [18]. It has been shown in [7] that the non-triplet harmonics $6r \pm 1$ where $r \in \{1, 2, 3, ...\}$ of the magneto-motive force (MMF) of a SDT machine are mapped to the fundamental $\alpha\beta$ subspace. In that case, the two dominant LOHs are the 5th and 7th components. This conclusion did not consider, however, the effect of winding's coil span (i.e. full-pitched or chorded).

Unlike full-pitched coil, the MMF distribution of chorded coils become asymmetrical over the stator periphery (i.e. over the north and south poles), which induces even space harmonics in the MMF spectra. For balanced $\alpha\beta$ stator excitation, this MMF asymmetry of individual coils has nothing to do with the total MMF distribution. For machines with symmetrical air-gap, these even harmonics influence neither the induced armature voltage nor the generated torque; as the contribution to the total average flux due to these harmonics over a full pole-pitch will add to zero [17], [20]. Correspondingly, even harmonic current components are usually not present. On the other hand, odd air-gap flux density harmonics contribute only to the induced armature voltage. For a reluctance rotor and given its highly non-linear characteristics [11], the effect of these even harmonics should, therefore, be carefully addressed, which is a main objective of this paper.

Using the prototype stator employed in this study having a 36-slot, 4-pole symmetrical six-phase double-layer winding assuming full-pitched coils and unit $\|i_\mathrm{s}^{dq}\| = 1$ p.u. excitation, the MMF spectrum is shown in Fig. 2(a), while the total MMF due to a unit xy current component in this case adds to zero. As is clear from Fig. 2(a), employing full-pitched coils for a winding with $\pi/3$ phase belt will introduce notable 5th and 7th MMF space harmonics. Therefore, a suitable selection of the coil span is 7/9 (commonly used for this slot number and termed the *optimum chording angle*), which would minimize the dominant LOHs. Figs. 2(b)-(c) show the MMF spectra of
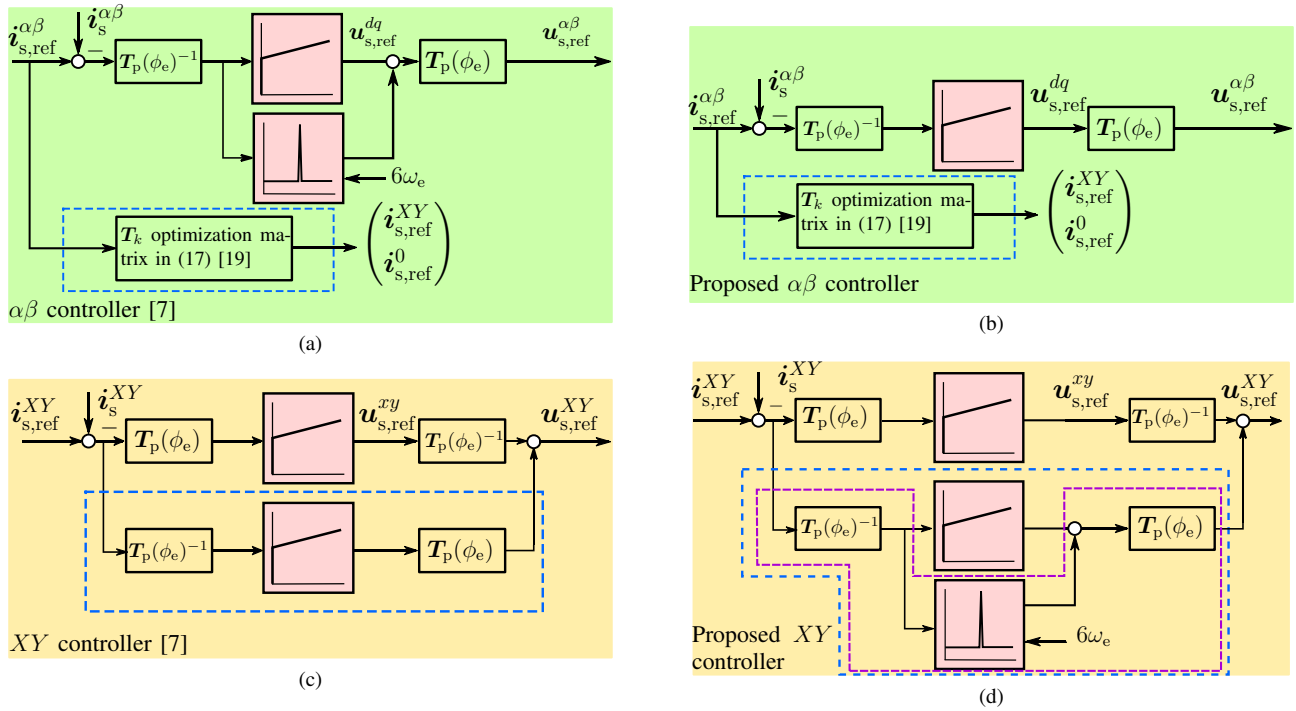
Fig. 4. Pre- and post-fault current controllers of the (a)-(b) $\alpha\beta$ and (c)-(d) XY subspaces, where (a) and (c) are as given by [7], while (b) and (d) are the proposed controllers. The highlighted blocks, PI and R controllers in ⌐ ⌐ are enabled only in the post-fault case, which are discussed in Section V, while the highlighted R controller in ⌐ ⌐ is activated additionally when computing the flux linkage ψ_s^{xy} as described in Section III-A.

7/9 chorded windings under unit i_s^{dq} and i_s^{xy} current components, respectively. Clearly, under xy excitation, the MMF distribution experiences even harmonics with notable magnitudes (the 2nd harmonic is approximately 30% of fundamental component). From winding function theory, the air-gap flux distribution can simply be approximated by the product of the MMF distribution with the inverse air-gap function [20], which eventually leads to an air-gap flux density spectra with similar harmonic spectra for cylindrical rotors. Hence, the notable even harmonics, especially the 2nd harmonic in Figs. 3(a)-(b), are introduced in the air-gap flux density distribution without inducing corresponding harmonic voltage components across different phases. Therefore, under xy excitation, the introduced even harmonics have no effect on the induced stator voltage. They only, however, contribute to the leakage flux component. Moreover, the rotor saliency of the SDT-RSM will further distort the air-gap flux density distribution and the air-gap flux spectrum will experience both odd (especially the 5th harmonic) and even harmonics when the rotor is running (see ▮ highlight in Fig. 3(b)). If the air-gap saliency and chorded winding arrangement would be neglected as in [7], one would overlook the presence of odd harmonics associated with xy subspace excitation (see ▮ highlight in Fig. 3(a)-(b)). This would prompt harmonic components in the event of i_s^{xy} injection as in the post-fault case in Section V. In conclusion, to improve the flux distribution of symmetrical six-phase machines, stator windings with chorded coils are used to suppress the 5th and 7th harmonics mapped to the $\alpha\beta$ subspace. However, the winding chording will introduce both even and odd harmonics, under xy excitation with salient pole rotors as in SDT-RSM. Therefore, a harmonic compensation

of low order odd harmonics should be introduced in the xy subspace. FE simulations are provided in Section VI to validate the effect of xy subspace excitation and the generation of low order harmonics.

As explained in [7], the presence of low-order odd harmonics in the $\alpha\beta$ subspace is similar to the three-phase harmonic mapping. However, such harmonics can be significantly reduced during the rewinding process from three to dual three-phase. For the same machine, when doubling the number of phases at a constant rated power, halving either the rated voltage or current is considered a degree of freedom. Halving the rated current, which is the one followed in this paper, will eventually double the circuit inductance compared to that of the original three-phase machine. Thus, the contribution of the odd harmonics will decrease in the $\alpha\beta$ subspace owing to the increase in the circuit impedance. Based on the aforementioned discussion and winding layout, the control in the $\alpha\beta$ frame can be dedicated only to regulate the fundamental component, while the low-order harmonics mapped to the XY subspace would be compensated only during post-fault operation, where $i_s^{XY} \neq 0$, or during flux linkage maps identification (shown later in Section III-A). These conclusions propose the control structure in Figs. 4(b) and (d), which is different than that proposed in literature for SDT drives, as proposed in [7], and shown in Fig. 4(a) and (c). It is worth to mention that if the optimum chording angle was not applied, the $\alpha\beta$ controller will encompass significant 5th and 7th harmonics requiring their compensation (see Fig. 4(a)). Nevertheless, the XY control structure would remain as proposed in Fig. 4(b). Table I summarizes the findings in Section II with respect to the harmonic mapping and its comparison to that in [7].
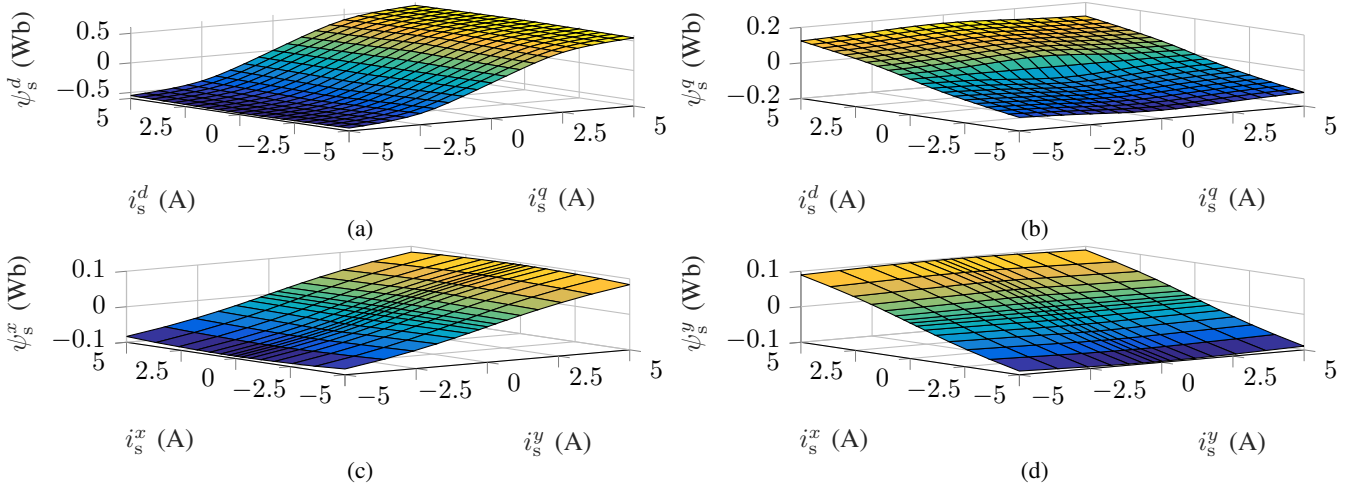
Fig. 5. Measured flux linkage maps of {(a),(b)} $\boldsymbol{\psi}_\mathrm{s}^{dq}$ for $||\boldsymbol{i}_\mathrm{s}^{dq}|| \leq \hat{i}_\mathrm{s,rated}$ and {(c),(d)} $\boldsymbol{\psi}_\mathrm{s}^{xy}$ for $||\boldsymbol{i}_\mathrm{s}^{xy}|| \leq \hat{i}_\mathrm{s,rated}$.

TABLE I. Harmonic mapping summary for the SDT-RSM with the proposed rewinding as in Section II and its comparison with that in [7].

Subspace	Harmonics [7]	Section II
$\alpha\beta$	$6r \pm 1$, where $r \in \{1, 2, 3, ...\}$	Neglected
XY	Neglected	$6r \pm 1$, where $r \in \{1, 2, 3, ...\}$
zero	$3h$, where $h \in \{1, 3, 5, ...\}$	

TABLE II. Parameters of the employed SDT-RSM drive.

Parameter	Value
Stator resistance	$R_\mathrm{s} = 2.51\,\Omega$
Pole-pair	$n_\mathrm{p} = 2$
Rated peak stator current	$\hat{i}_\mathrm{s,rated} = 5$ A
Rated torque	$m_\mathrm{e,rated} = 9.6$ N·m
Inertia	$\Theta = 94 \times 10^{-4}$ kg·m^2
Rated mechanical speed	3000 RPM
Sampling and switching frequencies	$f_\mathrm{sw} = 8$ kHz

III. FLUX LINKAGE MAPS IDENTIFICATION

Owing to the highly non-linear flux variations in RSMs [11], identifying such non-linearities is essential to ensure high performance torque control and optimal tuning of the current controllers which leads eventually to fast dynamics [21]. This is carried out through identifying the *flux-linkage maps* of the different subspaces, in a similar manner to those identified for asymmetrical DT-PMSM in [4].

Using the transformation $\boldsymbol{T}_\mathrm{VSD}$ in (1), while applying the synchronously rotating Park transformation,

$$\boldsymbol{T}_\mathrm{p}(\phi_\mathrm{e})^{-1} = \begin{bmatrix} \cos(\phi_\mathrm{e}) & \sin(\phi_\mathrm{e}) \\ -\sin(\phi_\mathrm{e}) & \cos(\phi_\mathrm{e}) \end{bmatrix}, \quad (3)$$

to the $\alpha\beta$ subspace and the anti-synchronous transformation $\boldsymbol{T}_\mathrm{p}(-\phi_\mathrm{e})^{-1} = \boldsymbol{T}_\mathrm{p}(\phi_\mathrm{e})$ to the XY subspace, the SDT-RSM dynamic model is

$$\left. \begin{aligned} \boldsymbol{u}_\mathrm{s}^{dq} &= R_\mathrm{s} \boldsymbol{i}_\mathrm{s}^{dq} + \omega_\mathrm{e} \boldsymbol{J} \boldsymbol{\psi}_\mathrm{s}^{dq} + \tfrac{\mathrm{d}}{\mathrm{d}t} \boldsymbol{\psi}_\mathrm{s}^{dq} \\ \boldsymbol{u}_\mathrm{s}^{xy} &= R_\mathrm{s} \boldsymbol{i}_\mathrm{s}^{xy} - \omega_\mathrm{e} \boldsymbol{J} \boldsymbol{\psi}_\mathrm{s}^{xy} + \tfrac{\mathrm{d}}{\mathrm{d}t} \boldsymbol{\psi}_\mathrm{s}^{xy} \\ \boldsymbol{u}_\mathrm{s}^{0} &= R_\mathrm{s} \boldsymbol{i}_\mathrm{s}^{0} + \tfrac{\mathrm{d}}{\mathrm{d}t} \boldsymbol{\psi}_\mathrm{s}^{0} \\ \tfrac{\Theta}{n_\mathrm{p}} \tfrac{\mathrm{d}\omega_\mathrm{e}}{\mathrm{d}t} &= \underbrace{3\, n_\mathrm{p} \boldsymbol{i}_\mathrm{s}^{dq\top} \boldsymbol{J} \boldsymbol{\psi}_\mathrm{s}^{dq}}_{=:m_e} - m_\mathrm{load} \end{aligned} \right\}, \quad (4)$$

where the drive parameters are shown in Table II. For a given subspace at steady-state, to identify the contribution of the current components to the corresponding flux linkages, one has to ensure that such current coordinates are orthogonal and independently controlled without exciting the remaining subspaces [11].

A. $\boldsymbol{\psi}_\mathrm{s}^{dq}$ and $\boldsymbol{\psi}_\mathrm{s}^{xy}$ flux linkage identification

Using the control structure in Fig. 4(b), setting $\boldsymbol{i}_\mathrm{s}^{xy} = 0$ (i.e. $\boldsymbol{i}_\mathrm{s,ref}^{XY} = 0$) in Fig. 4(d) and operating with a 2N connection (i.e. $\boldsymbol{i}_\mathrm{s}^{0} = 0$), one can at steady-state rewrite the dq dynamics in (4) as

$$\boldsymbol{\psi}_\mathrm{s}^{dq} = \frac{\boldsymbol{J}^{-1}}{\omega_\mathrm{e}} (\boldsymbol{u}_\mathrm{s}^{dq} - R_\mathrm{s} \boldsymbol{i}_\mathrm{s}^{dq}), \quad (5)$$

where for a given $\boldsymbol{i}_\mathrm{s}^{dq}$, controller output $\boldsymbol{u}_\mathrm{s}^{dq}$ and $\omega_\mathrm{e} \neq 0$, the flux linkage $\boldsymbol{\psi}_\mathrm{s}^{dq}$ can be computed. Sweeping $\boldsymbol{i}_\mathrm{s}^{dq}$ within the interval $||\boldsymbol{i}_\mathrm{s}^{dq}|| \leq \hat{i}_\mathrm{s,rated}$, the corresponding $\boldsymbol{\psi}_\mathrm{s}^{dq}$ is computed and plotted as in Figs. 5(a)-(b). The differential inductance matrix[1] defined as

$$\boldsymbol{L}_\mathrm{s}^{dq} = \begin{bmatrix} \frac{\partial \psi_\mathrm{s}^d}{\partial i_\mathrm{s}^d} & \frac{\partial \psi_\mathrm{s}^d}{\partial i_\mathrm{s}^q} \\ \frac{\partial \psi_\mathrm{s}^q}{\partial i_\mathrm{s}^d} & \frac{\partial \psi_\mathrm{s}^q}{\partial i_\mathrm{s}^q} \end{bmatrix} = \begin{bmatrix} L_\mathrm{s}^d & L_\mathrm{m}^{dq} \\ L_\mathrm{m}^{dq} & L_\mathrm{s}^q \end{bmatrix} \quad (6)$$

is computed from $\boldsymbol{\psi}_\mathrm{s}^{dq}$, processed using Matlab, and employed within the tuning of the current controller, as shown later in Section IV-A. A similar procedure is repeated to estimate the variation of $\boldsymbol{\psi}_\mathrm{s}^{xy}$ with respect to $\boldsymbol{i}_\mathrm{s}^{xy}$ within the interval $||\boldsymbol{i}_\mathrm{s}^{xy}|| \leq \hat{i}_\mathrm{s,rated}$, while setting $\boldsymbol{i}_\mathrm{s,ref}^{dq} = 0$. The employed control structure for the xy subspace is depicted in Fig. 4(d) with the activation of the R controller in ⌐¬; to compensate for the LOHs. Accordingly the differential inductances L_s^d, L_s^q, and the cross-coupling inductance L_m^{dq} are shown in Figs. 6(a)-(c), respectively, while L_s^x, L_s^y, and L_m^{xy} are shown in Figs. 7(a)-(c), respectively, as in [4], [11].

[1] Details on nonlinear modelling and the use of differential inductances in electrical drives can be found in [22, Chap. 14].
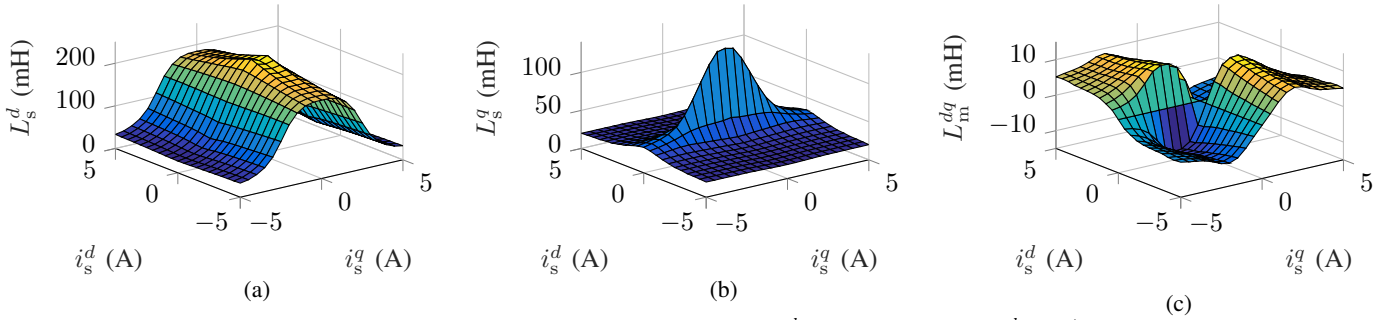
Fig. 6. Measured differential inductances of (a) L_s^d (b) L_s^q (c) L_m^{dq} within the domain $||\boldsymbol{i}_s^{dq}|| \leq \hat{i}_{s,\text{rated}}$.
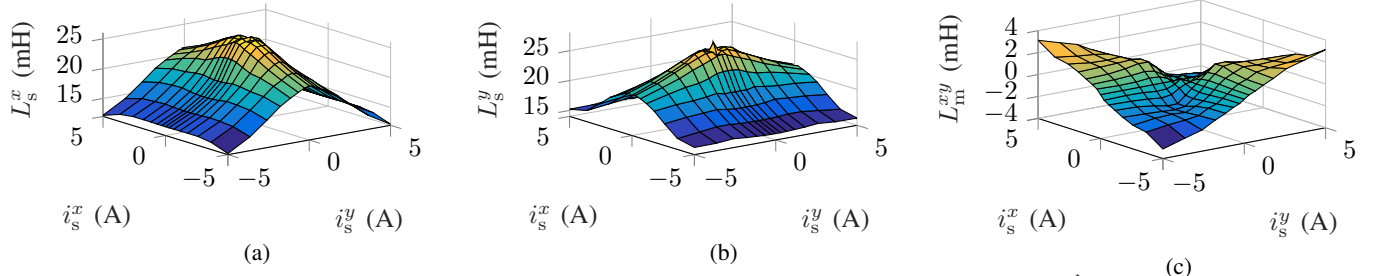
Fig. 7. Measured differential inductances of (a) L_s^x (b) L_s^y (c) L_m^{xy} within the domain $||\boldsymbol{i}_s^{xy}|| \leq \hat{i}_{s,\text{rated}}$.

B. Zero flux linkage

For asymmetrical drives, the 0^+0^- coordinates of the *zero* subspace components (i.e. triplet harmonics) are deemed orthogonal through a series connection of the phases belonging to the same three phase sets; leading to successful identification of $\boldsymbol{\psi}_s^0$ with respect to $\boldsymbol{i}_s^0$, such that $||\boldsymbol{i}_s^0|| \leq \hat{i}_{s,\text{rated}}$ [4]. On the other hand, it is impossible for SDT drives to configure a hardware connection; which would eventually lead to an orthogonal space variation between $\psi_s^{0^+}$ and $\psi_s^{0^-}$ as in [4], [23]; since triplet components are out-of-phase (i.e. π phase shift). In other words, identifying the *zero* flux linkage vector $\boldsymbol{\psi}_s^0$ within the interval $||\boldsymbol{i}_s^0|| \leq \hat{i}_{s,\text{rated}}$, similar to the procedures in [4], is inapplicable. Nevertheless, it is permissible to assume in advance that the *zero* subspace inductances L_s^{0+} and L_s^{0-} would not significantly vary in the interval $||\boldsymbol{i}_s^0|| \leq \hat{i}_{s,\text{rated}}$, as with L_s^x and L_s^y for $||\boldsymbol{i}_s^{xy}|| \leq \hat{i}_{s,\text{rated}}$ [4]. Accordingly, the hardware connection in Fig. 8 is proposed to estimate L_s^{0+} and L_s^{0-} by connecting the voltage-source inverter (VSI) terminals $\boxed{1}$ $\boxed{2}$ with $\boxed{\zeta_1}$ $\boxed{\zeta_2}$ or $\boxed{\lambda_1}$ $\boxed{\lambda_2}$, respectively. Even though the *zero* subspace coordinates are not orthogonal, such connections allows still to independently control the currents in both windings without exciting the other subspaces (i.e. $\boldsymbol{v}_s^{\alpha\beta} = \boldsymbol{v}_s^{XY} \overset{(1)}{=} 0$ since $v_s^{a\gamma} = v_s^{b\gamma} = v_s^{c\gamma}$ for $\gamma \in \{1, 2\}$). Thus, one can asses the variation severity of the inductances L_s^{0+} and L_s^{0-} with respect to $\boldsymbol{i}_s^0$. The relation between the VSI applied voltages, phase and subspace currents is

$$\left.\begin{array}{rcl} u_s^{\text{VSI}\gamma} &=& u_s^{a\gamma} + u_s^{b\gamma} + u_s^{c\gamma} \overset{(1)}{=} 3u_s^\Gamma, \\ i_s^{a\gamma} &=& i_s^{b\gamma} = i_s^{c\gamma} \Rightarrow i_s^\Gamma \overset{(1)}{=} i_s^{a\gamma}, \end{array}\right\} \quad (7)$$

where $\Gamma \in \{0^+, 0^-\}$. Neglecting the coupling between the 0^+0^- coordinates (i.e. as in L_m^{xy} in comparison with L_s^x and L_s^y in Fig. 7) and R_s as a known parameter, voltages of determined frequency are applied to each three-phase set separately and the phase shift between the applied voltage and the stator currents are measured. This is mathematically
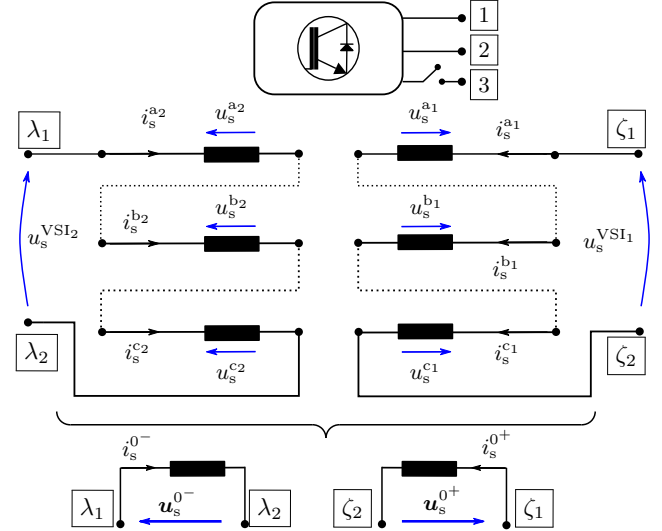
Fig. 8. Hardware connection for identifying the inductances L_s^{0+} and L_s^{0-}. Connecting the terminals $\boxed{1}$ $\boxed{2}$ with $\boxed{\zeta_1}$ $\boxed{\zeta_2}$ allows to compute L_s^{0+}, while the connection with $\boxed{\lambda_1}$ $\boxed{\lambda_2}$ allows to compute L_s^{0-}.

represented by

$$\left.\begin{array}{rcll} u_s^{\text{VSI}\gamma} &=& \hat{u}\cos(\omega_{\text{VSI}}t), & \forall \hat{u} > 0, \\ i_s^\Gamma &=& \hat{i}\cos(\omega_{\text{VSI}}t + \phi_L), & \forall \hat{i} > 0, \end{array}\right\} \quad (8)$$

where $\hat{i}$ is the amplitude of the current at steady-state, ω_{VSI} is the arbitrary angular frequency of the applied voltage by the VSI and ϕ_L is the phase shift angle, through which the corresponding inductances are estimated. Table III shows the corresponding results by running the SDT-RSM externally at $\omega_e = 100\,\text{rad/s}$, while exciting each three-phase set separately. It is observed that the inductances L_s^{0+} and L_s^{0-} are not significantly affected by the flowing currents. Thus, it is acceptable to consider that L_s^{0+} and L_s^{0-} are both constants, as indicated by the average values in Table III. Moreover, the test was repeated to estimate L_s^{0+} and L_s^{0-}, while exciting simultaneously the

TABLE III. Tests to estimate L_s^{0+} and L_s^{0-} in Fig. 8 at $\omega_\mathrm{e} = 100$ rad/s.

Connect $\boxed{1} \to \boxed{\zeta_1}$ and $\boxed{2} \to \boxed{\zeta_2}$ to estimate L_s^{0+}				
$\hat{u}$ (V)	$\hat{i}$ (A)	ω_VSI (rad/s)	ϕ_L (rad)	L_s^{0+} (mH)
7.25	1.0	60	0.12	5.02
63.23	5.0	60	0.932	5.39
				Average: 5.21
Connect $\boxed{1} \to \boxed{\lambda_1}$ and $\boxed{2} \to \boxed{\lambda_2}$ to estimate L_s^{0-}				
$\hat{u}$ (V)	$\hat{i}$ (A)	ω_VSI (rad/s)	ϕ_L (rad)	L_s^{0-} (mH)
7.9	1.0	60	0.1138	4.746
61.6	5.0	60	0.913	5.173
				Average: 4.96

Fig. 9. Estimated torque parabolas along with the MTPA loci confined within the designated rated current $\hat{i}_\mathrm{s,rated}$ loci, as indicated in Table II.

opposite three-phase set by $\hat{i} = 5$ A (i.e. estimating L_s^{0+} while $i_\mathrm{s}^{0-} = 5\cos(\omega_\mathrm{VSI}t + \phi_L)$, and vice versa). The corresponding outcome for each inductance did not exceed 4% than the average values in Table III, indicating that the cross-coupling between the 0^+0^- can be neglected.

IV. PROPOSED CURRENT CONTROLLER

A. Current controllers

The identified flux linkage maps and the corresponding differential inductances are employed for tuning the fundamental proportional-integral (PI) regulators in Figs. 4(b) and 4(d). The output of the the PI block diagram in Figs. 4(b) and 4(d) comprise both the output of the PI controller as well as the feedforward disturbance compensation terms. This is mathematically denoted by

$$\left.\begin{aligned} \boldsymbol{u}_\mathrm{s,ref}^{dq} &= \boldsymbol{u}_\mathrm{s,PI}^{dq} + \boldsymbol{u}_\mathrm{s,dist}^{dq}, \\ \boldsymbol{u}_\mathrm{s,ref}^{xy} &= \boldsymbol{u}_\mathrm{s,PI}^{xy} + \boldsymbol{u}_\mathrm{s,dist}^{xy}, \end{aligned}\right\} \quad (9)$$

where the tuning of the PI controller is discussed in Section IV-A1 and the feedforward compensation is shown in Section IV-A2

1) PI controller tuning: The tuning strategy is designed according to the magnitude optimum criterion along with parametrizing the PI controller gain and time constant per every $\boldsymbol{i}_\mathrm{s}^{dq}$ [11]. Thus, the proportional gain V_p and integral time constant T_i of the PI controllers in the dq and xy frames in Figs. 4(b) and 4(d) are adaptively tuned as follows

$$\left.\begin{aligned} \left(V_p^d,\ V_p^q,\ V_p^x,\ V_p^y\right) &= \tfrac{f_\mathrm{sw}}{2}\left(\hat{L}_\mathrm{s}^d,\ \hat{L}_\mathrm{s}^q,\ \hat{L}_\mathrm{s}^x,\ \hat{L}_\mathrm{s}^y\right), \\ \left(T_i^d,\ T_i^q,\ T_i^x,\ T_i^y\right) &= \tfrac{1}{R_\mathrm{s}}\left(\hat{L}_\mathrm{s}^d,\ \hat{L}_\mathrm{s}^q,\ \hat{L}_\mathrm{s}^x,\ \hat{L}_\mathrm{s}^y\right), \end{aligned}\right\} \quad (10)$$

where

$$\left.\begin{aligned} \left(\hat{L}_\mathrm{s}^d,\ \hat{L}_\mathrm{s}^q\right) &= \det\!\left(\boldsymbol{L}_\mathrm{s}^{dq}(\boldsymbol{i}_\mathrm{s}^{dq})\right)\left(\tfrac{1}{L_\mathrm{s}^q},\ \tfrac{1}{L_\mathrm{s}^d}\right), \\ \left(\hat{L}_\mathrm{s}^x,\ \hat{L}_\mathrm{s}^y\right) &= \det\!\left(\boldsymbol{L}_\mathrm{s}^{xy}(\boldsymbol{i}_\mathrm{s}^{xy})\right)\left(\tfrac{1}{L_\mathrm{s}^y},\ \tfrac{1}{L_\mathrm{s}^x}\right). \end{aligned}\right\} \quad (11)$$

The tuning of the *zero* subspace proportional-resonant (PR) controller follows the same procedure as in (10) with the only exception, that the inductance variations in the *zero* subspace are neglected. Thus, the PR controller is tuned by

$$\left.\begin{aligned} \left(V_\mathrm{p}^{0+},\ V_\mathrm{p}^{0-}\right) &= \tfrac{f_\mathrm{sw}}{2}\left(L_\mathrm{s}^{0+},\ L_\mathrm{s}^{0-}\right), \\ \left(T_\mathrm{i}^{0+},\ T_\mathrm{i}^{0-}\right) &= \tfrac{1}{R_\mathrm{s}}\left(L_\mathrm{s}^{0+},\ L_\mathrm{s}^{0-}\right). \end{aligned}\right\} \quad (12)$$

2) Feedforward disturbance compensation: To further enhance the dynamics of the dq and xy subspaces, decoupling the coordinates based on the identified $\boldsymbol{\psi}_\mathrm{s}^{dq}$ and $\boldsymbol{\psi}_\mathrm{s}^{xy}$ is employed [11]. The disturbance voltage $\boldsymbol{u}_\mathrm{s,dist}^{dq}$ encompasses the coupling terms between the dq coordinates, which is computed by

$$\boldsymbol{u}_\mathrm{s,dist}^{dq} = -L_\mathrm{m}^{dq}\begin{bmatrix} 0 & \frac{1}{\hat{L}_\mathrm{s}^q} \\ \frac{1}{\hat{L}_\mathrm{s}^d} & 0 \end{bmatrix}\left(\boldsymbol{u}_\mathrm{s}^{dq} - R_\mathrm{s}\,\boldsymbol{i}_\mathrm{s}^{dq} - \omega_\mathrm{e}\,\boldsymbol{J}\boldsymbol{\psi}_\mathrm{s}^{dq}\right) - \omega_\mathrm{e}\,\boldsymbol{J}\boldsymbol{\psi}_\mathrm{s}^{dq}. \quad (13)$$

Note that $\boldsymbol{u}_\mathrm{s,dist}^{dq}$ is added to the output of the PI controllers, but not shown in Fig. 4(b). Similarly, the decoupling between the xy coordinates, similar to (13), is

$$\boldsymbol{u}_\mathrm{s,dist}^{xy} = -L_m^{xy}\begin{bmatrix} 0 & \frac{1}{\hat{L}_\mathrm{s}^y} \\ \frac{1}{\hat{L}_\mathrm{s}^x} & 0 \end{bmatrix}\left(\boldsymbol{u}_\mathrm{s}^{xy} - R_\mathrm{s}\,\boldsymbol{i}_\mathrm{s}^{xy} - \omega_\mathrm{e}\,\boldsymbol{J}\boldsymbol{\psi}_\mathrm{s}^{xy}\right) + \omega_\mathrm{e}\,\boldsymbol{J}\boldsymbol{\psi}_\mathrm{s}^{xy}. \quad (14)$$

The presence of 5th and 7th harmonics in the XY subspace (i.e. 6th harmonic in the xy subspace) is considered a disturbance, requiring a resonant (R) controller (see Fig. 4(d)) to compensate such disturbance. The R controller in the xy subspace is enabled only when $\boldsymbol{i}_\mathrm{s}^{xy} \neq 0$, which is the case when computing the flux linkage $\boldsymbol{\psi}_\mathrm{s}^{xy}$ or in the post-fault operation as explained in Sections III-A and V, respectively.

B. Maximum-torque-per-ampere (MTPA)

Based on the identified $\boldsymbol{\psi}_\mathrm{s}^{dq}$ in Fig. 5(a)-(b) and using (4), it is possible to estimate the *torque map*, which is a four quadrant plot showing the torque m_e in both motoring and generating modes over $\boldsymbol{i}_\mathrm{s}^{dq}$ within the interval $\|\boldsymbol{i}_\mathrm{s}^{dq}\| \leq \hat{i}_\mathrm{s,rated}$ [21]. Fig. 9 depicts the first-quadrant (i.e. motor quadrant) of the aforementioned plot. For every torque parabola in Fig. 9, it is possible to compute the point of minimum current magnitude $\|\boldsymbol{i}_\mathrm{s}^{dq}\|$, which would eventually lead to the MTPA loci (see —○— in Fig. 9). Unlike the MTPA plots for RSM obtained in [24], the MTPA plot in Fig. 9 accounts for all possible values of $\|\boldsymbol{i}_\mathrm{s}^{dq}\| \leq \hat{i}_\mathrm{s,rated}$. As expected, the rated current $\hat{i}_\mathrm{s,rated}$ in Fig. 9 corresponds to the rated torque $m_\mathrm{e,rated}$ (see Table II), as verified experimentally in Section VI. Moreover, for a given reference torque $m_\mathrm{e,ref}$ and using the MTPA loci, the corresponding reference currents
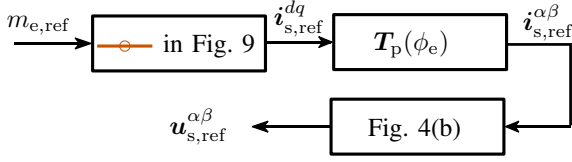
Fig. 10. Torque controller of the SDT-RSM, where the $m_{\text{e,ref}}$ is translated into $\boldsymbol{i}_{\text{s,ref}}^{dq}$ using the MTPA loci in Fig. 9. The current $\boldsymbol{i}_{\text{s,ref}}^{\alpha\beta}$ is fed into Fig. 4(b).
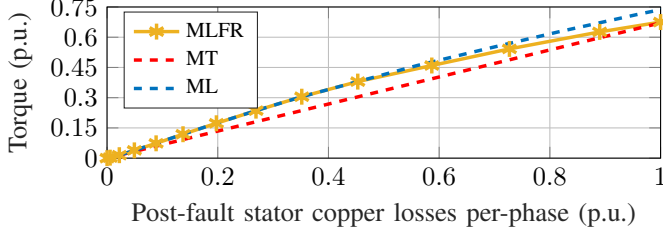
Fig. 11. Comparison between the torque and the corresponding stator power losses upon applying the different optimization strategies.

$\boldsymbol{i}_{\text{s,ref}}^{dq}$ are dispatched to the underlying current controller in Fig. 4(b) (i.e. $\boldsymbol{i}_{\text{s,ref}}^{\alpha\beta} = \boldsymbol{T}_{\text{p}}(\phi_{\text{e}})^{-1}\boldsymbol{i}_{\text{s,ref}}^{dq}$) as indicated in Fig. 10. Furthermore, the estimated MTPA loci $\boldsymbol{i}_{\text{s}}^{dq}$ will be employed in the post-fault operation as shown in the upcoming section.

V. POST-FAULT OPERATION

The study of fault tolerance is often addressed in literature assuming that the fault has been cleared, which leads to one or more open-phases [8], [12], [15], [19], [25]. This is also known as open-phase fault. In literature, three possible post-fault operating strategies exist: minimum stator losses (ML), maximum torque (MT), and the minimum losses full-range (MLFR) [8], [15], [25]. The ML optimization constraints minimize the total stator Joule losses for a given reference torque, leading to limited torque-production capability and unequal loading of different phases [25]. MT equalizes the losses for the remaining healthy phases up to the rated current value, which eventually maximizes the produced electromagnetic torque at the expense of higher total copper losses, compared to ML [25]. The MLFR optimization was recently developed only for the asymmetrical DT drives. It combines the merits of ML and MT, where minimum losses would be ensured up to the maximum torque realized by the MT strategy [15]. Moreover, it is possible to further manipulate the MLFR to include the drive voltage limits within the optimization constraints [19]. The currents $\boldsymbol{i}_{\text{s,ref}}^{XY}$ and $\boldsymbol{i}_{\text{s,ref}}^{0}$ in [19] are set at *steady state* dependant on $\boldsymbol{i}_{\text{s,ref}}^{\alpha\beta}$ (see Fig. 4(b)), depending on the neutral configuration (i.e. 1N or 2N) and the faulty phases, to achieve the optimization objectives.

From a mathematical perspective, $\boldsymbol{i}_{\text{s,VSD}}$ can be related to $\boldsymbol{i}_{\text{s}}^{\alpha\beta}$ at *steady state* in the post-fault case as [12], [15] by

$$\begin{pmatrix} \boldsymbol{i}_{\text{s,ref}}^{\alpha\beta} \\ \boldsymbol{i}_{\text{s,ref}}^{XY} \\ \boldsymbol{i}_{\text{s,ref}}^{0} \end{pmatrix} = \underbrace{\begin{bmatrix} 1 & 0 \\ 0 & 1 \\ k_X^{\alpha} & k_X^{\beta} \\ k_Y^{\alpha} & k_Y^{\beta} \\ -1-k_X^{\alpha} & -k_X^{\beta} \\ 1+k_X^{\alpha} & k_X^{\beta} \end{bmatrix}}_{=:\boldsymbol{T}_k \in \mathbb{R}^{6\times 2}} \boldsymbol{i}_{\text{s,ref}}^{\alpha\beta}, \quad (15)$$
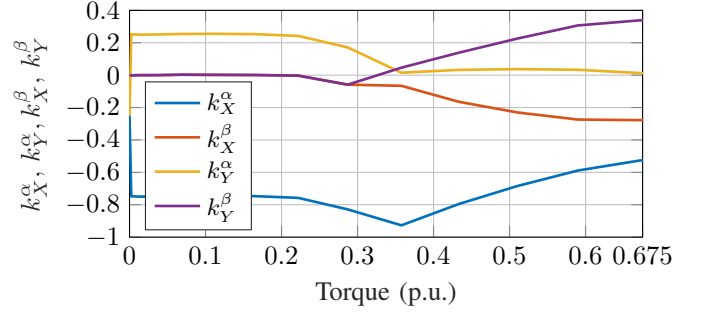
Fig. 12. Variation of elements of the optimization matrix $\boldsymbol{T}_k$ with respect to post-fault torque for the MLFR strategy.

TABLE IV. Outcome summary of the optimization in (16) and (17) showing the matrix elements $\boldsymbol{T}_k$ with respect to ML, MT, and MLFR.

$\boldsymbol{T}_k$ elements	ML	MT	MLFR
k_X^{α}	-0.75	-0.53	
k_X^{β}	0	-0.28	see Fig. 12
k_Y^{α}	0.255	0.01	
k_Y^{β}	0	0.34	

where $\boldsymbol{T}_k$ is the optimization matrix consisting of its scalar parameters k_X^{α}, k_X^{β}, k_Y^{α}, and k_Y^{β} when running the *fmincon* optimizer in Matlab upon passing the cost function and its constraints as seen shortly. Considering only one open-circuit fault in this study and following in the footsteps of [12], [15] by defining the sets of phases as $\mathbb{S} \in \{a_1, ..., c_2\}$, faulty phases $\mathbb{S}_f$ and the healthy phases $\mathbb{S}_h := \mathbb{S} \setminus \mathbb{S}_f$ (i.e. $\mathbb{S}_h \cap \mathbb{S}_f = \varnothing$); the objective function to minimize the stator copper losses p_{Cu} is written as

$$\min_{\boldsymbol{T}_k} \; p_{\text{Cu}} = \frac{(\boldsymbol{i}_{\text{s}}^{\mathbb{S}_h})^{\top} \boldsymbol{i}_{\text{s}}^{\mathbb{S}_h}}{6(i_{\text{s,rated}})^2}, \quad (16)$$

subject to the following constraints:

$$\left.\begin{array}{ll} g_1: & i_{\text{s}}^{\rho_f} = 0, \; \forall \rho_f \in \mathbb{S}_f \\ g_2: & \displaystyle\sum_{\rho_h \in \mathbb{S}_h} i_{\text{s}}^{\rho_h} = 0, \\ g_3: & m_{\text{e}} = m_{\text{e,ref}}, \\ g_4: & \begin{cases} \hat{i}_{\text{s}}^{\rho_h} = \hat{i} \le \hat{i}_{\text{s,rated}}, \; \forall \rho_h \in \mathbb{S}_h & \text{MT case,} \\ \|\boldsymbol{i}_{\text{s}}^{\mathbb{S}_h}\|_{\infty} \le \hat{i}_{\text{s,rated}} & \text{MLFR case,} \\ \text{Discard} & \text{ML case,} \end{cases} \end{array}\right\} \quad (17)$$

where the constraint g_4 is (i) discarded for the ML case, (ii) ensures for the MT case that the remaining phases would carry equal currents up to $\hat{i}_{\text{s,rated}}$, or (iii) manipulates $\boldsymbol{T}_k$ for the MLFR optimization such that remaining phase currents would saturate one after the other and not exceed $\hat{i}_{\text{s,rated}}$. Even though such optimizations are, in principle, applicable for SDT drives by utilising the transformation in (1) instead of that for asymmetrical DT in [15], [25], the main contributions of this paper to the SDT-RSM post-fault operation are:

- Taking into account the non-linearity of the SDT-RSM by adopting the MTPA loci in Fig. 9, which will be the basis for the ML, MT, and MLFR post-fault optimizations. The corresponding results are shown in Fig. 11 for each strategy with the corresponding elements of the $\boldsymbol{T}_k$ matrix in Table IV and Fig. 12. The maximum permissible post-
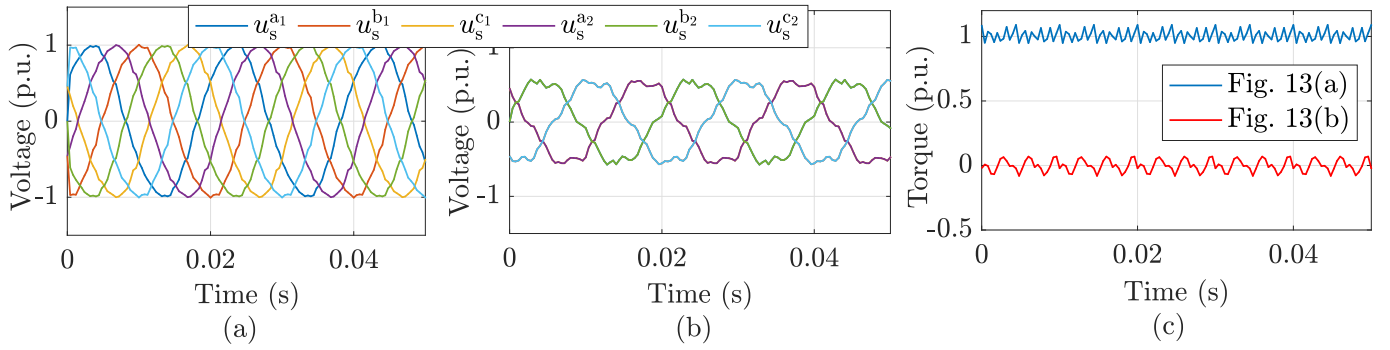
Fig. 13. FE simulation showing the stator voltages at (a) $\|\boldsymbol{i}_s^{dq}\|$=1 p.u. excitation and (b) $\|\boldsymbol{i}_s^{xy}\|$=1 p.u. and the resulting m_e for each case in (c).
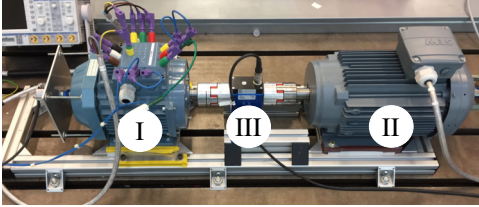
Fig. 14. Test bench: (I) SDT-RSM, (II) induction machine (i.e. prime mover) and (III) torque sensor.

fault torque $m_{e,max}$ is 0.675 p.u., which is less than that of 0.771 p.u. for SDT-PMSM drives with 1N connection in the unified fault tolerant analyses in [8]. This is due to the fact that for RSM drives, a portion of the current vector $\boldsymbol{i}_s^{dq}$ is used for magnetizing the machine, and accordingly results in a lower torque $m_{e,max}$; and

• Proposing the control structure highlighted in ⌐¬⌐ in Figs. 4(b) and 4(d), owing to the harmonic mapping discussed in Section II-B. The significant 5th and 7th harmonics in the XY subspace (i.e. 6th harmonic in the xy subspace) are compensated by means of the R controller, tuned at $6\omega_e$, which lead to acceptable performance as seen later in the experimental results. The controllers within ⌐¬⌐ are triggered only in the post-fault operation.

VI. EVALUATION RESULTS

A. Finite element simulations

First, the FE simulation is carried-out to theoretically explain the effect of the rotor saliency on the harmonic mapping. The simulation was executed by rotating the machine at 1500 rpm with a 2N configuration, while exciting the stator with 1 p.u. currents once via the $\alpha\beta$ subspace, while the other time via XY subspace. The corresponding stator voltages are shown in Figs 13(a)-(b), respectively. Exciting the $\alpha\beta$ subspace resulted in almost harmonic-free phase voltages u_s^κ, where $\kappa \in \{a_1, b_1, c_1, a_2, b_2, c_2\}$; owing to the rewinding technique followed as explained in Section. II-B. It is concluded that controlling only the fundamental component in the $\alpha\beta$ subspace would be sufficient (see Fig. 4(b)) without the need of employing resonant (R) controllers for the LOHs as in [7] (see Fig. 4(a)). On the other hand, exciting the XY subspace lead to the generation of the LOHs in such subspace. Using an opposite analogy, applying fundamental voltages in the XY subspace without harmonic controllers would lead

to substantial generation of LOHs. This depicts the need for harmonic R controllers (see Fig. 4(d)), if such subspace is to be excited, as in the post-fault operation.

B. Experimental validation

1) Test-bench description: From a practical validation perspective, the test bench in Fig. 14 was set-up consisting of a SDT-RSM (in torque-controlled mode) coupled to a three-phase induction machine acting as prime mover (i.e. speed controlled). Both machines share the same DC-link voltage and are controlled via the field-oriented control structure. Using Matlab/Simulink, the control algorithm is implemented on a dSPACE DS1007 board. The PWM signals are sent to the VSIs via the DS5101 PWM card, where the triggering signals are manually programmed to ensure precise timings and sampling instants. The A/D DS2004 board is triggered by the DS5101 board to carry-out the measurements in the middle of the switching period. The SDT-RSM control structure is as depicted in Fig. 1, where the reference voltages $\boldsymbol{u}_{s,ref}^{\alpha\beta}$ and $\boldsymbol{u}_{s,ref}^{XY}$ are the outputs of the their corresponding controllers in Figs. 4(c) and 4(d), respectively. The implemented PI controllers of the SDT-RSM are tuned as explained in Section IV-A with the aid of the flux linkage and differential inductances in Figs. 5-7. The resonant controllers are discretized via the impulse-invariant method to ensure stability and precise lock on the tuned resonant frequency [26].

2) Experimental results: Fig. 15 verifies the MTPA loci when setting the $m_{e,ref} = m_{e,rated}$ at a 2N connection in a healthy operation, while the $\alpha\beta$ and the XY control structures were as shown in Figs. 4(b) and 4(d), respectively. Fig. 15(a) shows that the desired torque reference was generated via regulating $\boldsymbol{i}_s^{dq}$ in Fig. 15(b) and correspondingly the stator currents $\boldsymbol{i}_s^{a_1 \to c_2}$ in Fig. 15(c), which concludes that R controllers are not needed in the healthy case with a 2N connection. The corresponding flux linkages $\boldsymbol{\psi}_s^{dq}$ and $\boldsymbol{\psi}_s^{xy}$ are shown in Fig 15(d). On the other hand, by exciting the XY subspace (or xy subspace), as shown in Fig. 16 using the suggested control structure of [7] in Fig. 4(c), led to the generation of LOHs (mainly the 5th and 7th harmonics). Increasing the flow of currents in the XY subspace will give rise to substantial increase of the harmonic content in $i_s^{a_1}$ as seen in Figs 16(b)-(d). Employing the proposed control structure in Fig. 4(d) will compensate such LOHs for the same $\boldsymbol{i}_s^{xy}$ excitation, as seen in Figs. 17(a)-(d). The xy flux linkage $\boldsymbol{\psi}_s^{xy}$
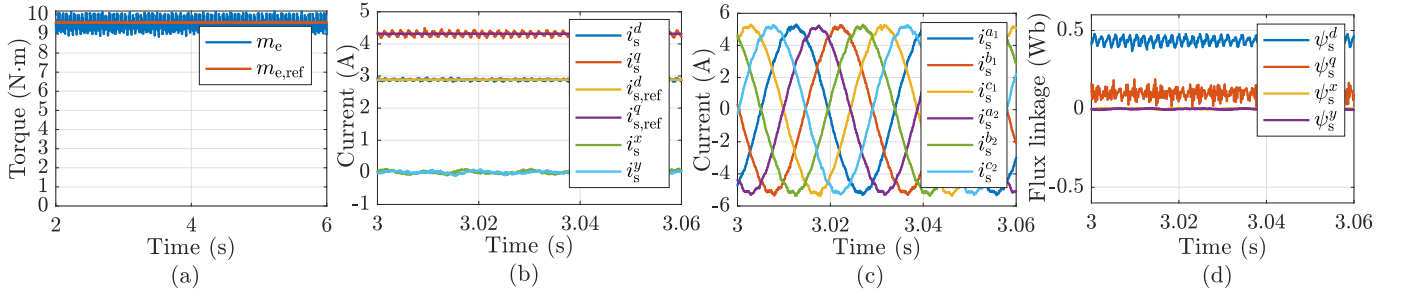
Fig. 15. Pre-fault stator currents at $m_{\mathrm{e,rated}}$ corresponding to the MTPA criteria when applying the proposed rewinding with 2N configuration and only PI controllers in the dq- and xy-subspaces: (a) Reference and measured torque, (b) $\boldsymbol{i}_{\mathrm{s,ref}}^{dq}$ and $\boldsymbol{i}_{\mathrm{s}}^{dq}$, (c) $\boldsymbol{i}_{\mathrm{s}}^{a_1 \to c_2}$, and (d) $\boldsymbol{\psi}_{\mathrm{s}}^{dq}$ and $\boldsymbol{\psi}_{\mathrm{s}}^{xy}$.
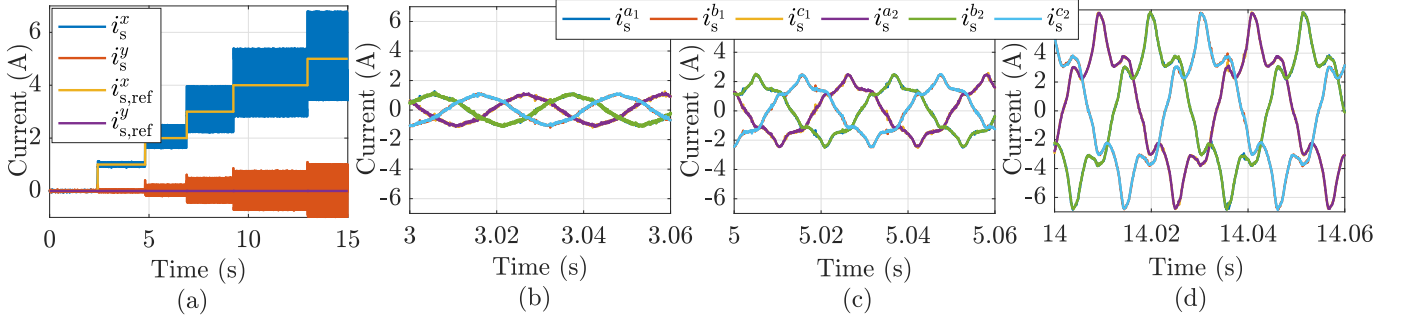
Fig. 16. Effect of different $\boldsymbol{i}_{\mathrm{s}}^{xy}$ current injections and the harmonics associated with the stator currents at 1000 rpm: (a) $\boldsymbol{i}_{\mathrm{s,ref}}^{xy}$ and $\boldsymbol{i}_{\mathrm{s}}^{xy}$, and (b)-(d) the corresponding $\boldsymbol{i}_{\mathrm{s}}^{a_1 \to c_2}$. The xy control structure in [7] (see Fig. 4(c)) is employed in this test.
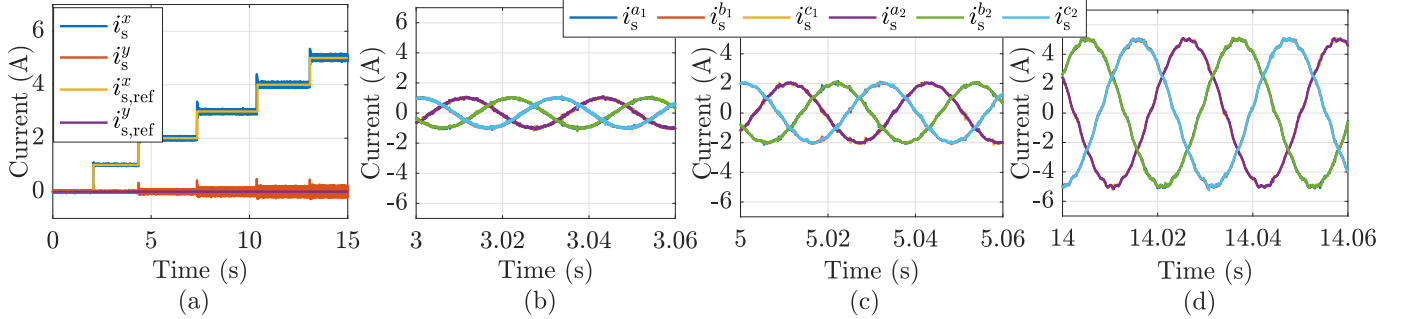
Fig. 17. Effect of different $\boldsymbol{i}_{\mathrm{s}}^{xy}$ current injections along with harmonic compensation (see R-controller highlighted in [dashed box] in Fig. 4(d)) in the xy subspace showing the stator currents 1000 rpm: (a) $\boldsymbol{i}_{\mathrm{s,ref}}^{xy}$ and $\boldsymbol{i}_{\mathrm{s}}^{xy}$, and (b)-(d) the corresponding $\boldsymbol{i}_{\mathrm{s}}^{a_1 \to c_2}$.
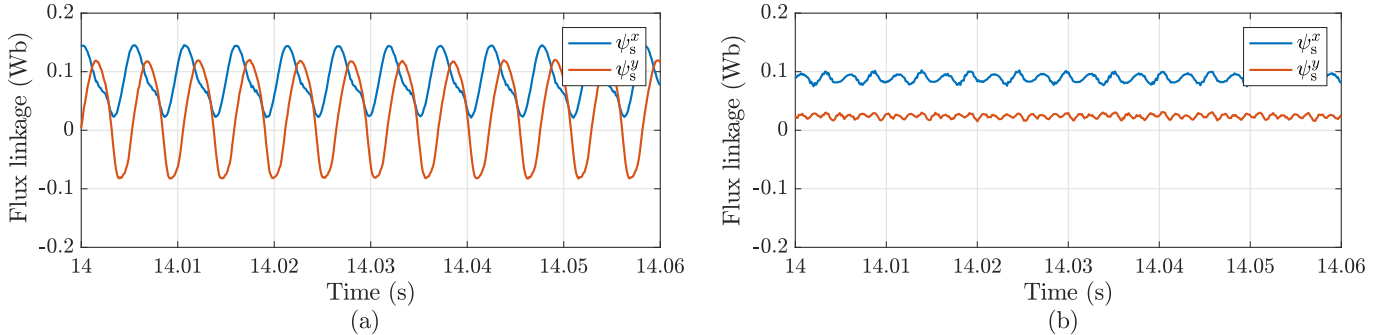
Fig. 18. The flux linkage $\boldsymbol{\psi}_{\mathrm{s}}^{xy}$ corresponding to $\boldsymbol{i}_{\mathrm{s}}^{xy} = (5, 0)$ A within the interval $14 \leq t \leq 14.06$ s in (a) Fig. 16(d) and (b) Fig. 17(d).

corresponding to the currents $\boldsymbol{i}_{\mathrm{s}}^{xy}$ in Figs. 16(d) and 17(d) are indicated in Figs. 18(a) and (b), respectively. Such plots confirm the outcomes of Section II-B that the 6$^{\mathrm{th}}$ harmonic would evolve in the xy subspace for any $\boldsymbol{i}_{\mathrm{s}}^{xy}$ excitation. Furthermore, Figs. 18(a) and (b) depict the coupling between xy coordinates, where $\psi_{\mathrm{s}}^y \neq 0$ for $\boldsymbol{i}_{\mathrm{s}}^{xy} = (5, 0)$ A, unlike the assumption of decoupled ψ_{s}^x and ψ_{s}^y in the available body of literature [5]–[7], [12], [15].

For testing the MLFR post-fault operation in Fig. 11, the

circuit breaker of phase a_1 was deliberately disconnected (i.e. $i_{\mathrm{s}}^{\mathrm{a}_1} = 0$). The neutral point connection 1N was configured owing to its higher torque-per-ampere characteristic in comparison with the 2N configuration [8], [19]. Combining the control structure of the $\alpha\beta$ and the XY subspaces in Figs. 15(b) and 15(d), respectively, with the *zero* subspace controller in Fig. 1, high quality stator currents were observed in Figs. 19(a) and 19(b), which correspond to $m_{\mathrm{e}} = 0.1$ p.u. and $m_{\mathrm{e}} = m_{\mathrm{e,max}} = 0.675$ p.u. in Figs. 19(c) and 19(d),
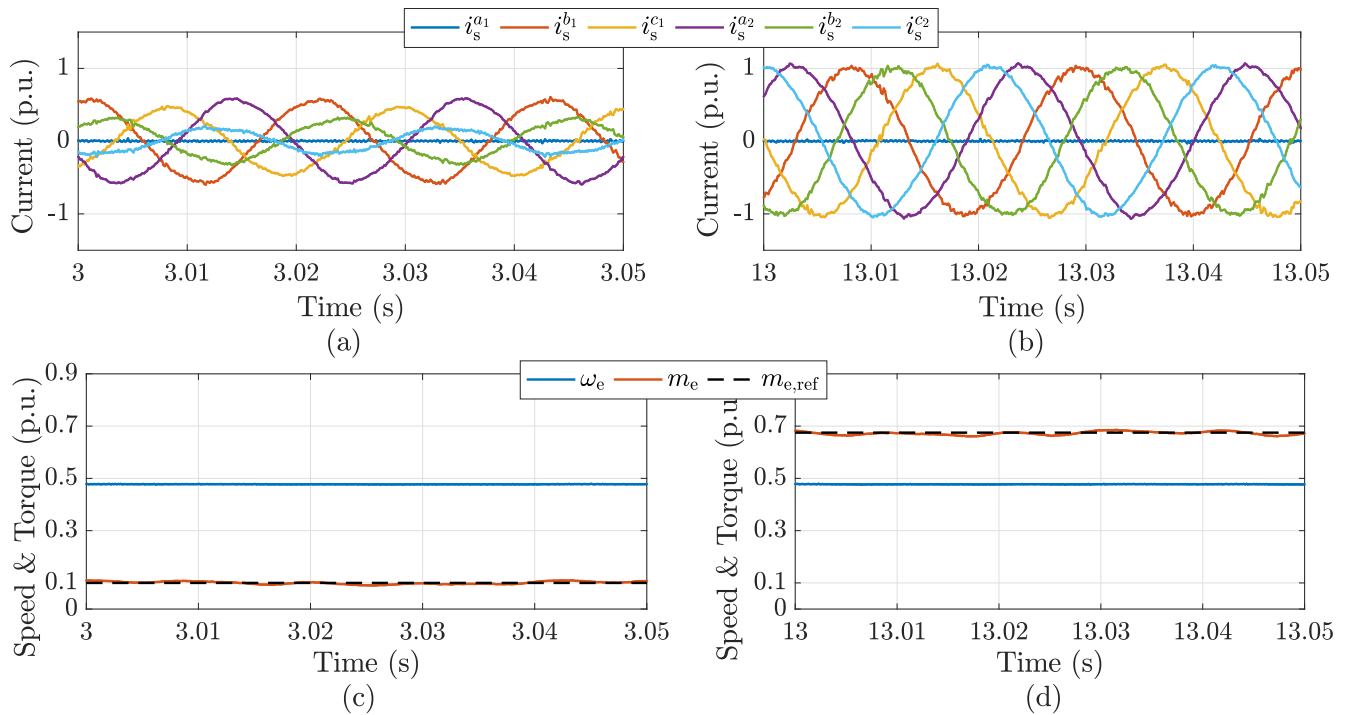
Fig. 19. Post-fault operation for the 1N connection at $\omega_e = 0.478$ p.u. corresponding to the MLFR optimization in [19] at showing the stator currents of the healthy phases at (a) $m_e = 0.1$ p.u. and (b) $m_{e,\max} = 0.675$ p.u. as well as the measured mechanical quantities in (c) and (d), respectively.

respectively. In Fig. 19(a), the stator currents are of unequal magnitude; since a torque reference $m_{e,ref} = 0.1$ p.u. for the MLFR corresponds to a ML optimization (see Fig. 11), while the current magnitudes in Fig. 19(b) correspond to $m_{e,\max}$, which is the maximum operating point for the MT strategy.

VII. CONCLUSION

This paper presented a different methodology in identifying the harmonics related to every subspace of a SDT-RSM drive, where its importance is inevitable to ensure high performance post-fault operation. Employing a double layer stator winding with chorded coils and an optimal chording angle waived the need for harmonic controllers in the healthy 2N case, unlike the proposed control structures available in literature. Even if the optimum chording angle was not applied, both the $\alpha\beta$ and XY subspaces of the SDT-RSM comprise the 5th and 7th harmonics. In that particular case, the $\alpha\beta$ controller should compensate such harmonics, similar to the control structure given in literature. Upon identifying the non-linear flux linkages in the $\alpha\beta$ subspace, the torque map is estimated, which takes into account the effects of cross-coupling and saturation. Based on the estimated torque maps, the MTPA loci were identified, which were used in both the pre and the post-fault operations. Combining the proposed control structure with the available recent post-fault optimization strategy, it is possible to ensure a high quality of stator currents in the pre and post-fault cases. FE simulations were provided to verify the proposed harmonic mapping. The theoretical findings were corroborated on 3 kW test bench, where experimental results have been carried out for the sake of validation.

REFERENCES

[1] E. Levi, "Multiphase electric machines for variable-speed applications," *IEEE Trans. on Ind. Electron.*, vol. 55, pp. 1893–1909, May 2008.

[2] E. Levi, R. Bojoi, F. Profumo, H. A. Toliyat, and S. Williamson, "Multiphase induction motor drives - a technology status review," *IET Electr. Power Appl.*, vol. 1, pp. 489–516, July 2007.

[3] K. Marouani, L. Baghli, D. Hadiouche, A. Kheloui, and A. Rezzoug, "A new pwm strategy based on a 24-sector vector space decomposition for a six-phase vsi-fed dual stator induction motor," *IEEE Trans. on Ind. Electron.*, vol. 55, pp. 1910–1920, May 2008.

[4] H. M. Eldeeb, A. S. Abdel-Khalik, and C. M. Hackl, "Dynamic modeling of dual three-phase IPMSM drives with different neutral configurations," *IEEE Trans. on Ind. Electron.*, vol. 66, pp. 141–151, Jan 2019.

[5] Y. Hu, Z. Q. Zhu, and K. Liu, "Current control for dual three-phase permanent magnet synchronous motors accounting for current unbalance and harmonics," *IEEE Journal of Emerging and Selected Topics in Power Electron.*, vol. 2, pp. 272–284, June 2014.

[6] H. S. Che, E. Levi, M. Jones, W. P. Hew, and N. A. Rahim, "Current control methods for an asymmetrical six-phase induction motor drive," *IEEE Trans. on Power Electron.*, vol. 29, pp. 407–417, Jan 2014.

[7] A. G. Yepes, J. Malvar, A. Vidal, O. López, and J. Doval-Gandoy, "Current harmonics compensation based on multiresonant control in synchronous frames for symmetrical$n$-phase machines," *IEEE Trans. on Ind. Electron.*, vol. 62, pp. 2708–2720, May 2015.

[8] W. N. W. A. Munim, M. Duran, H. S. Che, M. Bermudez, I. Gonzalez-Prieto, and N. A. Rahim, "A unified analysis of the fault tolerance capability in six-phase induction motor drive," *IEEE Trans. on Power Electron.*, vol. 32, no. 10, pp. 7824–7836, 2016.

[9] A. G. Yepes, J. Doval-Gandoy, F. Baneira, D. Perez-Estevez, and O. Lopez, "Current harmonic compensation for n-phase machines with asymmetrical winding arrangement and different neutral configurations," *IEEE Trans. on Ind. Appl.*, vol. PP, no. 99, pp. 1–1, 2017.

[10] B. Wang, J. Wang, B. Sen, A. Griffo, Z. Sun, and E. Chong, "A fault-tolerant machine drive based on permanent magnet-assisted synchronous reluctance machine," *IEEE Tran. on Ind. Appl.*, vol. 54, pp. 1349–1359, March 2018.

[11] C. M. Hackl, M. J. Kamper, J. Kullick, and J. Mitchell, "Current control of reluctance synchronous machines with online adjustment of the controller parameters," in *in Proceedings of the 2016 IEEE International Symposium on Ind. Electron. (ISIE 2016)*, (Santa Clara, CA, USA), pp. 156–160, 2016.

[12] A. G. Yepes, J. Doval-Gandoy, F. Baneira, and H. Toliyat, "Control strategy for dual three-phase machines with two open phases providing minimum loss in the full torque operation range," *IEEE Transactions on Power Electronics*, 2018 (doi:10.1109/TPEL.2018.2830507).

[13] I. Gonzalez-Prieto, M. J. Duran, H. S. Che, E. Levi, M. Bermúdez, and F. Barrero, "Fault-tolerant operation of six-phase energy conversion systems with parallel machine-side converters," *IEEE Trans. on Power Electron.*, vol. 31, pp. 3068–3079, April 2016.

[14] W. Wang, J. Zhang, M. Cheng, and S. Li, "Fault-tolerant control of dual three-phase permanent-magnet synchronous machine drives under open-phase faults," *IEEE Trans. on Power Electron.*, vol. 32, pp. 2052–2063, March 2017.

[15] F. Baneira, J. Doval-Gandoy, A. G. Yepes, Ó. López, and D. Pérez-Estévez, "Control strategy for multiphase drives with minimum losses in the full torque operation range under single open-phase fault," *IEEE Trans. on Power Electron.*, vol. 32, pp. 6275–6285, Aug 2017.

[16] T. Lipo, "A d-q model for six phase induction machines," in *Proceedings of the Int. Conf. Electric Machines*, pp. 860–867, 1980.

[17] E. A. Klingshirn, "High phase order induction motors - part i-description and theoretical considerations," *IEEE Trans. on Power Apparatus and Systems*, vol. PAS-102, pp. 47–53, Jan 1983.

[18] X. B. Bomela and M. J. Kamper, "Effect of stator chording and rotor skewing on performance of reluctance synchronous machine," *IEEE Trans. on Ind. Appl.*, vol. 38, pp. 91–100, Jan 2002.

[19] H. M. Eldeeb, A. S. Abdel-Khalik, and C. M. Hackl, "Post-fault full torque-speed exploitation of dual three-phase ipmsm drives," *IEEE Trans. on Ind. Electron.*, 2018 (early access, doi: 10.1109/TIE.2018.2880698).

[20] S. M. Raziee, O. Misir, and B. Ponick, "Winding function approach for winding analysis," *IEEE Trans. on Magnet.*, vol. 53, pp. 1–9, Oct 2017.

[21] H. Eldeeb, C. M. Hackl, L. Horlbeck, and J. Kullick, "A unified theory for optimal feedforward torque control of anisotropic synchronous machines," *International Journal of Control*, pp. 1–30, June 2017. (open access doi:10.1080/00207179.2017.1338359).

[22] C. M. Hackl, *Non-identifier based adaptive control in mechatronics: Theory and Application*. No. 466 in Lecture Notes in Control and Information Sciences, Berlin: Springer International Publishing, 2017.

[23] H. S. Che, A. S. Abdel-Khalik, O. Dordevic, and E. Levi, "Parameter estimation of asymmetrical six-phase induction machines using modified standard tests," *IEEE Trans. on Ind. Electron.*, vol. 64, no. 8, pp. 6075–6085, 2017.

[24] A. Yousefi-Talouki, P. Pescetto, G. Pellegrino, and I. Boldea, "Combined active flux and high-frequency injection methods for sensorless direct-flux vector control of synchronous reluctance machines," *IEEE Trans. on Power Electron.*, vol. 33, pp. 2447–2457, March 2018.

[25] H. S. Che, M. J. Duran, E. Levi, M. Jones, W. P. Hew, and N. A. Rahim, "Postfault operation of an asymmetrical six-phase induction machine with single and two isolated neutral points," *IEEE Trans. on Power Electron.*, vol. 29, pp. 5406–5416, Oct 2014.

[26] H. Eldeeb, A. Massoud, A. S. Abdel-Khalik, and S. Ahmed, "A sensorless kalman filter-based active damping technique for grid-tied vsi with lcl filter," *International Journal of Electrical Power & Energy Systems*, vol. 93, pp. 146 – 155, 2017.

Hisham M. Eldeeb received his B.Sc. (honors) and M.Sc. in electrical engineering in 2011, 2014, respectively, from the Faculty of Engineering, Alexandria University, Egypt. From 2012 to 2015, he worked as a research associate at Qatar University in Qatar, hired on a 1.4M$ project; aiming at extending the penetration of inverter-based distributed-generation plants within the Qatari-Network. From September 2015 to 2018, he pursued his PhD degree at the Technical University of Munich (TUM) in Germany and was selected as one of the 14 Marie-Curie Ph.D. candidates hired on the 3M€ EU Horizon H2020 project "Airborne Wind Energy System Control and Optimization" (AWESCO). He is currently working as an electrical drive specialist and development engineer for e-vehicles at IAV GmbH. His research interests are grid-connected converters, power electronics, and multi-phase drives.

Ayman S. Abdel-Khalik (SM'12) received the B.Sc. and M.Sc. degrees in electrical engineering from Alexandria University, Alexandria, Egypt, in 2001 and 2004, respectively, and the Ph.D. degree in electrical engineering from Alexandria University, and Strathclyde University, Glasgow, U.K., in 2009, under a dual channel program. He is currently an Associate Professor with the Electrical Engineering Department, Faculty of Engineering, Alexandria University, Alexandria, Egypt. He serves as an Associate Editor of IET Electric Power Applications Journal and the Executive Editor of Alexandria Engineering Journal. His current research interests include electrical machine design and modelling, electric drives, energy conversion, and renewable energy.

Julian Kullick was born in Aachen, Germany. He received the B.Sc. and M.Sc. degrees in electrical engineering from Technical University of Munich (TUM), Munich, Germany in 2012 and 2015 respectively. He is currently working toward the Ph.D. degree in electrical engineering with TUM. From 2015 to 2018 he was a Research Associate with the research group "Control of Renewable Energy Systems (CRES)" at TUM. Since 2019 he is a Research Associate with the "Laboratory for Mechatronic and Renewable Energy Systems (LMRES)", Munich University of Applied Sciences, Munich, Germany. His research interests include nonlinear modelling, efficient operation and sensorless control of electric drives.

Christoph M. Hackl (M'12 - SM'16) was born in 1977 in Mannheim, Germany. After studying electrical engineering (controls and mechatronics) at Technical University of Munich (TUM), Germany and University of Wisconsin-Madison, USA, he received the B.Sc., Dipl.-Ing., and Dr.-Ing. (Ph.D.) degree in 2003, 2004 and 2012, respectively, from TUM. Since 2004, he has been teaching electrical drives, power electronics, and mechatronic & renewable energy systems. Since 2014, he has been the head of the research group "Control of Renewable Energy Systems (CRES)" at TUM. In 2018, he became a Professor for Electrical Machines and Drives and the head of the "Laboratory for Mechatronic and Renewable Energy Systems (LMRES)" at the Munich University of Applied Sciences (MUAS), Germany. His main research interests include nonlinear, adaptive and optimal control of electrical, mechatronic and renewable energy systems.